Experimental validation of a purely analytical model dedicated to fuel cell diagnosis

A. PLAIT, F. DUBAS
Université de Franche-Comté, FEMTO-ST, FCLAB, UTBM, CNRS, Belfort, France

Highlights –
An analytical model is required to develop a diagnostic tool for fuel cells (FC) using magneto-tomography.
Magneto-tomography is an effective method to diagnose the health state of a FC.
Good agreement with experimental measurements permits to validate the multi-layer model.
Magneto-tomography using multi-layer model could consequently increase the FC lifetime.

Abstract –
The magnetic field distribution of an electromagnetic device could provide information about its health state. This paper focuses on the Fuel Cell (FC) diagnosis using the magneto-tomography, which involves mapping the magnetic field produced by any electrical device. Since magnetic field and current density are directly related, this study could describe the (ab)normal operation of a FC. For this purpose, a two-dimensional (2-D) multi-layer model based on Maxwell-Fourier methods is developed. In order to validate the developed model for the FC diagnosis, an experimental bench was set up to emulate the FC operating mode. This innovative purely analytical model presents confident results, the magnetic field generated by the FC is studied into three different functioning cases. The analytical results and the experimental measurements are similar in the three cases, in the worst situation, the difference of the magnetic field doesn't exceed 15 A/m, this is representing a relative error of 7%. The efficiency of the model is consequently established.

Keywords –

Fuel cell diagnosis

Analytical model

Experimental validation

Magneto-tomography

1. Introduction

Hydrogen energy offers interesting prospects, especially in an automotive application [1]-[2]. In a logic of economy, ecology and sustainability, it is necessary to increase the Fuel Cell (FC) lifetime. For this purpose, degradation mechanisms and impacts on FC degradation can be classified, especially in hybrid transport applications [3].

Many factors (e.g., obstruction of the gas diffusion layer, humidity, temperature hotspots, ...) can affect the current density distribution inside the FC and thus its performances. In order to diagnose the polymer exchange membrane fuel cell (PEMFC), many methods have been developed based on physical models [4]-[5] or experimental data [6]. Multiple techniques for assessing current density distribution have been documented in the literature [7]. These methods, however, exhibit drawbacks such as invasiveness, limited adaptability, and a lack of clarity regarding their impact on the measured current density distribution.

Contrary to invasive method, magneto-tomography consists of measuring the magnetic field distribution around a FC. This interesting non-invasive method allows for an efficient study of FC health state. Compared to conventional methods, the advantage lies in the fact that this method is non-invasive and has virtually no feedback effect on the tested object and the current density distribution to be measured. The approach is straightforward to implement, flexible, and proves to be reliable and practical within a controlled environment. Even if the presence of any system device could affect the amplitude and distribution of the generated magnetic field, it could be possible to using a faraday cage around the FC to limited the interference on the measurements. In addition to fuel cell research and development, other application areas encompass quality assurance in a production facility [8].

Hauer *et al.* (2005) [8] were the first to use this method for FC diagnosis. To estimate the health state of the FC using the magneto-tomography, the Biot-Savart law [8]-[12], varying-network magnetic circuit [12] or the heuristic search method [13]-[14] are used. Recently, Plait *et al.* (2020) [15] developed a new magnetic field analysis device to increase the diagnostic performance. During the last two decades, many research activities have been carried out in order to estimate the health state of the FC using the measurement of the magnetic field around the FC. In this way, Plait and Dubas (2022) [16] have provided an exhaustive review of the FC diagnosis by magneto-tomography.

The current methods for assessing the current density distribution by magneto-tomography can be broadly characterized as redundant, time-consuming, and exhibiting varying levels of accuracy. An innovative model (since no corresponding method exist in the literature) is developed in order to accentuate the efficiency of the method. The first step of the project is presented in this paper, which consists of the description and the experimental validation of the model. Biot & Savart law are fluently used in the literature but need regularization and conditioning to resolve the inverse problem. The proposed complex purely analytical model will permit to make a more accurate inverse resolution without manipulation but is not in the scope of this paper.

In this paper, a purely analytical magnetostatic model for the FC diagnosis is developed and validated by experimental measurements. In section 2, the purely and complex analytical multi-layer model is presented. There is currently no 2D multi-layer model based on the Maxwell-Fourier method in the existing literature for diagnosing a PEMFC (Proton Exchange Membrane Fuel Cell) stack. This approach relies on the formal solution of Maxwell's magnetostatic equations in Cartesian coordinates (x, y) through the utilization of the separation of variables method, Fourier series, and the superposition principle. This purely analytical multi-layer model has the potential to offer a comprehensive theoretical analysis of magnetic field distribution with a fast computational speed. Here, the magneto-tomographic study is

performed on a PEMFC stack in order to diagnose the health state. In section 3, the purely analytical model is validated using experimental measurements on a FC emulator. Some researchers have been already making first validation an emulator/simulator, which exhibit performant results as coherent as on real FC. The used experimental emulator presenting the possibility to make different configurations, consisting of 100 aluminum bars alimented by DC current, reproduces the behavior of a FC that will have different types/locations of failure and reflects the current density distribution. Around the FC, the generated magnetic field is measured by micro-Hall effect sensor placed at regular intervals around the FC. In the last section, the results obtained by the multi-layer analytical model are compared with the experimental measurements. A good accuracy between the results allows to diagnose and localize the possible defects. Furthermore, the capabilities of the model combined with the interesting results allow to consider many perspectives.

2. 2-D multi-layer model

2.1. FC consideration

A PEMFC stack, as illustrated in Fig. 1, is composed of several essential components, with the membrane serving as its core. This thin polymeric sheet plays a crucial role by selectively permitting the passage of protons while impeding the flow of electrons. As the chemical reaction unfolds, protons traverse the PEM, resulting in the generation of an electric current.

Situated on the positive side of the stack, the cathode often incorporates a catalytic material, such as platinum. This material facilitates the reduction of protons and electrons with oxygen, culminating in the formation of water. Conversely, the anode, located on the negative side, typically comprises a catalytic substance (e.g., platinum) that aids in the oxidation of hydrogen into protons and electrons.

The Gas Diffusion Layers (GDL) are strategically positioned on both sides of the cathode and anode. Their role is pivotal in facilitating the diffusion of gases (hydrogen on the anode side, oxygen or air on the cathode side) to the electrodes, while simultaneously permitting the exit of water produced during the chemical reaction.

Bipolar plates serve to separate each cell within the stack and play a dual role in distributing gases and electricity. Additionally, they can function as mechanical support and current collectors, further contributing to the overall efficiency and stability of the fuel cell system.

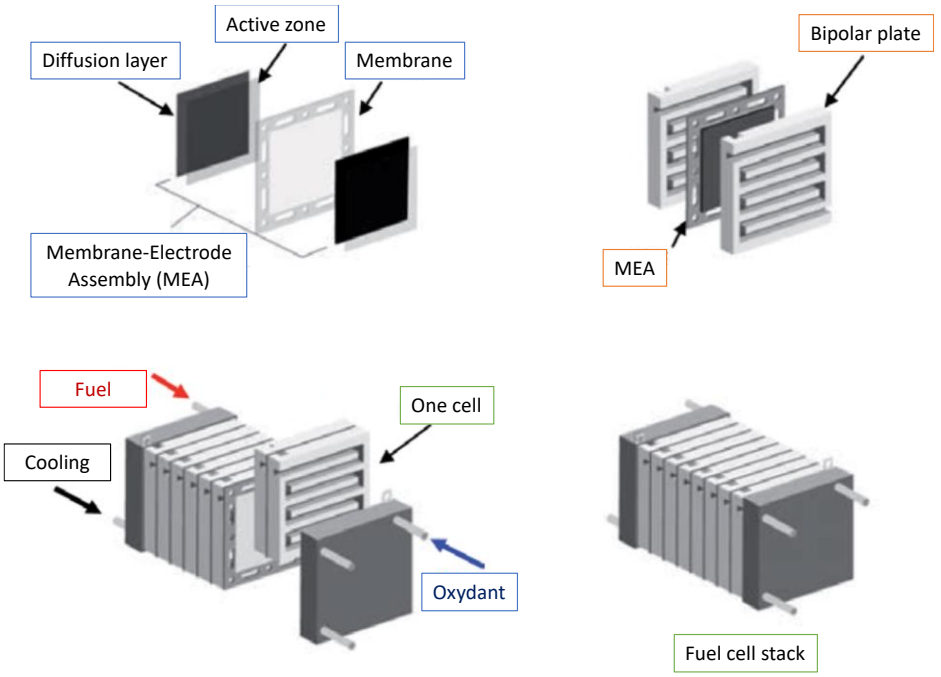

Fig. 1. FC stack considered.

If bipolar plates were made of magnetic materials, they can generate an internal magnetic field within the stack, but it's not always the case. The magnetic permeability of nearly all materials extensively employed in fuel cells is highly comparable to that of a vacuum. Besides, every component of the cell originally constructed with magnetic steel could be substituted by components crafted from non-magnetic materials, such as aluminum or stainless steel.

Concerning the geometric configuration, the specific arrangement of bipolar plates in the repetitive unit can create regions of magnetic field concentration or attenuation along the stack. This depends on the geometry of the plates and how they are spaced relative to each other. In this condition, each plate will produce a distinct current density map, it could be possible to repeat the measurements of the magnetic field along the stack with different mapping in order to recreate a quasi-3-D reconstruction.

Another condition, if the stack is exposed to external magnetic conditions as for example any another device of the system and near the stack, this could impact measurements. It could be rectified by adding a faraday cage in order to reduce this impact.

2.2. Magnetostatic study of a FC

A cell of a FC stack, exposed in Fig. 2, consists of a central active part (i.e., electrochemical active cell) and a surrounding inactive part (i.e., seal). The FC stack geometry considered is a ZSW product which proposing a surface active of 100 cm^2 (10 cm × 10 cm). The central active part can be decomposed into a multitude of segments. The 2-D magnetic field distribution of the FC bipolar plate was studied from multi-layer model by solving magnetostatic Maxwell's equations in Cartesian coordinates (x, y). Knowing the current density distribution inside the FC, it is possible to accurately estimate the magnetic field distribution generated around the FC, or vice versa (by solving an inverse problem).

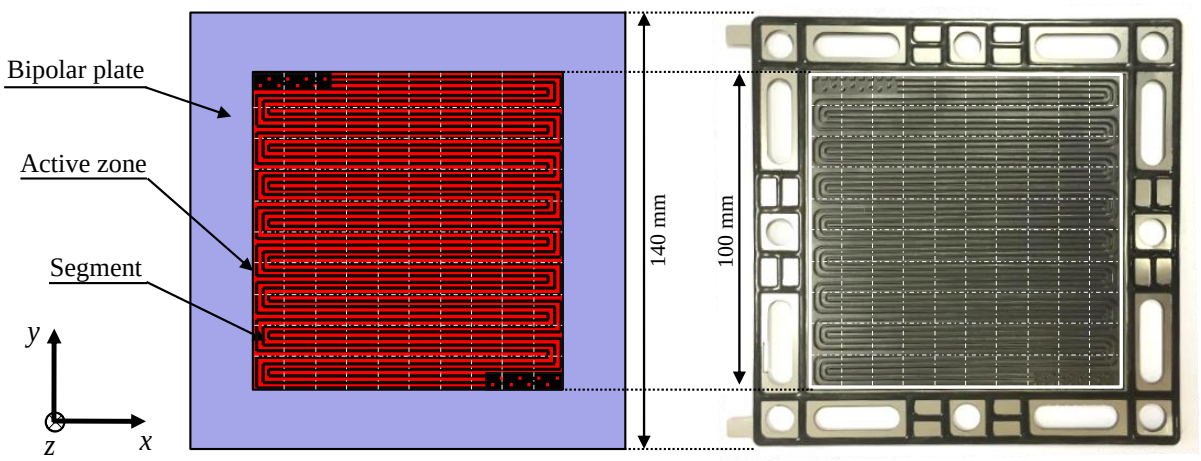

Fig. 2. ZSW FC and bipolar plate.

The modeling of a cell (bipolar plate) is decomposed into 3 regions, viz., (R1) and (R3) similar to vacuum and (R2) the electrochemical active cell, as shown in Fig. 3.

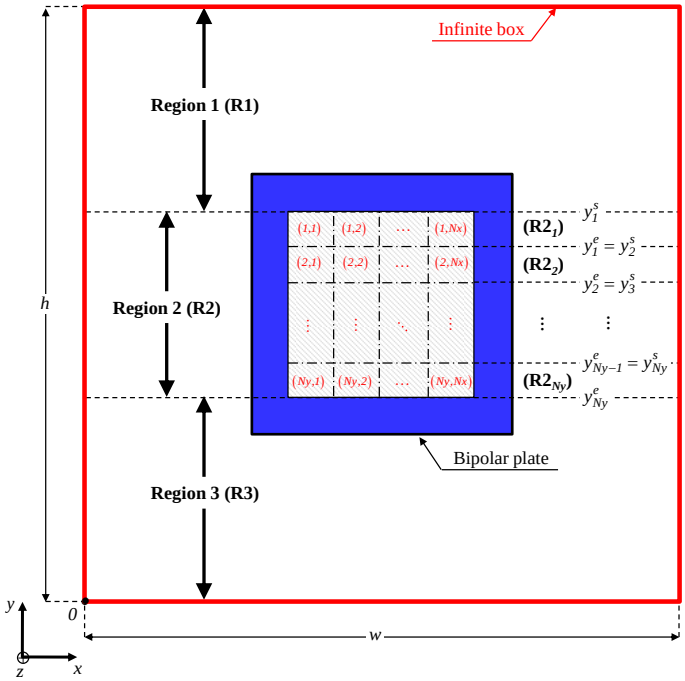

Fig. 3. FC bipolar plate modeling with 3 regions [16].

The complete original and general analytical model is detailed in [16]. But a new conceptualization with the main steps of the modeling is given as follows. The assumptions and the principal differential equation are reported.

The simplifying assumptions of the multi-layer analytical model are as follows:

- ✓ the end-effects are neglected (magnetic variables are independent of z);
- ✓ the magnetic vector potential and current density have only one component along the z-axis, i.e., $\boldsymbol{A} = \{0; 0; A_z\}$ and $\boldsymbol{J} = \{0; 0; J_z\}$;
- ✓ the skin depth effect is not considered;
- ✓ the absolute magnetic permeability μ of all components used in the bipolar plates of PEMFC stack are very close to the vacuum magnetic permeability $\mu_v = \mu_0$. In fact,

many industrial PEMFC stacks use graphite bipolar plates and non-magnetic stainless steels for rods and other mechanical parts [15].

2.3. Analytical resolution

In the quasi-stationary regime, the magnetostatic Maxwell's equations are embodied by Maxwell– Ampère. With the general assumptions of the study applied, within Cartesian coordinates (*x*,*y*), the general Partial Differential Equations (PDEs) governing magnetostatic in terms $\boldsymbol{A}=\{0;0;A_z\}$ inside an isotropic and uniform material (i.e., $\mu=C^{ste}$) can be formulated using the Laplace's, as represented by equation in (R1)

$$\Delta A_{z1}=\frac{\partial^2 A_{z1}}{\partial x^2}+\frac{\partial^2 A_{z1}}{\partial y^2}=0\,, \tag{1}$$

and in (R3)

$$\Delta A_{z3}=\frac{\partial^2 A_{z3}}{\partial x^2}+\frac{\partial^2 A_{z3}}{\partial y^2}=0\,, \tag{2}$$

and the Poisson's equation in (*R2*$_i$)

$$\Delta A_{z2_i}=\frac{\partial^2 A_{z2_i}}{\partial x^2}+\frac{\partial^2 A_{z2_i}}{\partial y^2}=-\mu_0\cdot J_{z2_i}\,, \tag{3}$$

where J_{z2_i} is the spatial distribution of $\boldsymbol{J}$ along the x-axis for each i, i.e., in (R2$_i$), which is defined by

$$J_{z2_i}=\sum_j J_{zij}=\sum_k J_{i,k}^{cs}\cdot sin\left(\beta_k\cdot x\right). \tag{4}$$

Applying Coulomb's gauge law derived from the Maxwell's equation, the components of $\boldsymbol{B}=\{B_x;B_y;0\}$ regardless of the region, can be deduced from A_z using the expression

$$B_x=\frac{\partial A_z}{\partial y}\ \text{and}\ B_y=-\frac{\partial A_z}{\partial x}\,. \tag{5}$$

From the magnetic material equation, $\boldsymbol{B}=\mu\cdot\boldsymbol{H}+\mu_0\cdot\boldsymbol{Mr}$, and according to the materials assumptions, the components of $\boldsymbol{H}=\{H_x;H_y;0\}$ are defined by $\boldsymbol{H}=\boldsymbol{B}/\mu_0$.

In problems involving electromagnetic fields, the overall solutions of regions rely on the Boundary Conditions (BC) established at the interface between two surfaces. These conditions are determined by the continuity of the parallel magnetic field $\boldsymbol{H}_{//}$ and $\boldsymbol{A}$ [40]. Within the infinite box [refer to Figure 3], the magnetic potential vector A_z adheres to the Dirichlet's BC, specially $A_z=0$.

By employing the separation of variables method, the 2D general solution for A within each region can be expressed by Fourier's series. The coefficients, which represent the unknowns or integration constants in the series, are determined analytically through a linear matrix system that satisfies the BCs.
To simplify the formal resolution of the Cramer's system, the superposition principle is applied to each sub-region *i* (*R2*$_i$).
In (R1) for $y\in\left[y_1^s,h\right]$ and $\forall x\in[0,w]$, the magnetic vector potential A_{z1}, a solution to equation (3) satisfying the various BCs, is defined as

$$A_{z1} = \sum_{i,k} \mu_0 \cdot \frac{J_{i,k}^{cs}}{\beta_k^{\,2}} \cdot D1_{i,k} \cdot f1_{i,k}(y) \cdot \sin(\beta_k \cdot x) \tag{6}$$

and the components of $\boldsymbol{H_1}$ (i.e., H_{x1} and H_{y1}) by

$$H_{x1} = -\sum_{i,k} \frac{J_{i,k}^{cs}}{\beta_k} \cdot D1_{i,k} \cdot g1_{i,k}(y) \cdot \sin(\beta_k \cdot x) \tag{7}$$

$$H_{y1} = -\sum_{i,k} \frac{J_{i,k}^{cs}}{\beta_k} \cdot D1_{i,k} \cdot f1_{i,k}(y) \cdot \cos(\beta_k \cdot x) \tag{8}$$

where

$$f1_{i,k}(y) = sh\left[\beta_k \cdot (h-y)\right] \Big/ sh\left[\beta_k \cdot \left(h - y_i^s\right)\right] \tag{9}$$

$$g1_{i,k}(y) = ch\left[\beta_k \cdot (h-y)\right] \Big/ sh\left[\beta_k \cdot \left(h - y_i^s\right)\right] \tag{10}$$

$$D1_{i,k} = NumD1_{i,k} / Den_{i,k} \tag{11}$$

with

$$Den_{i,k} = a1_k \cdot \left(a3_{i,k} - a4_{i,k}\right) + a3_{i,k} \cdot a4_{i,k} \cdot \left(a1_k^{\,2} + a2_k^{\,2}\right) - 1 \tag{12}$$

$$NumD1_{i,k} = -\left(a2_k + a1_k \cdot a4_{i,k} + 1\right) \tag{13}$$

in which

$$a1_k = -sh(\beta_k \cdot h_{cs}) / ch(\beta_k \cdot h_{cs}) \tag{14}$$

$$a2_k = -1 / ch(\beta_k \cdot h_{cs}) \tag{15}$$

$$a3_{i,k} = ch\left[\beta_k \cdot \left(h - y_i^s\right)\right] \Big/ sh\left[\beta_k \cdot \left(h - y_i^s\right)\right] \tag{16}$$

$$a4_{i,k} = -sh\left(\beta_k \cdot y_i^e\right) \Big/ ch\left(\beta_k \cdot y_i^e\right) \tag{17}$$

In equation (R3) for $y \in \left[0, y_{Ny}^e\right]$ and $\forall x \in [0, w]$, the magnetic vector potential A_{z3}, a solution to equation (2) that satisfies the specified boundary conditions, is defined as follows:

$$Den_{i,k} = a1_k \cdot \left(a3_{i,k} - a4_{i,k}\right) + a3_{i,k} \cdot a4_{i,k} \cdot \left(a1_k^{\,2} + a2_k^{\,2}\right) - 1 \tag{18}$$

and the components of $\boldsymbol{H_3}$ (H_{x3} and H_{y3}) by

$$H_{x3} = \sum_{i,k} \frac{J_{i,k}^{cs}}{\beta_k} \cdot D3_{i,k} \cdot g3_{i,k}(y) \cdot \sin(\beta_k \cdot x), \tag{19}$$

$$H_{y3} = -\sum_{i,k} \frac{J_{i,k}^{cs}}{\beta_k} \cdot D3_{i,k} \cdot f3_{i,k}(y) \cdot \cos(\beta_k \cdot x), \tag{20}$$

where

$$f3_{i,k}(y) = sh(\beta_k \cdot y) \Big/ ch\left(\beta_k \cdot y_i^e\right), \tag{21}$$

$$g3_{i,k}(y) = ch(\beta_k \cdot y) \Big/ ch\left(\beta_k \cdot y_i^e\right), \tag{22}$$

$$D3_{i,k} = NumD3_{i,k} / Den_{i,k}, \tag{23}$$

with

$$NumD3_{i,k} = -\left[a3_{i,k} \cdot \left(a1_k{}^2 + a2_k{}^2 \right) + a3_{i,k} \cdot a2_k - a1_k \right], \tag{24}$$

In equation (R2$_i$) for $y \in \left[y_i^e, y_i^s \right]$ and $\forall x \in [0, w]$, the magnetic vector potential A_{z2_i}, a solution to equation (3) that meets the specified boundary conditions, is expressed as:

$$A_{z2_i} = \sum_k \left\{ \sum_{n=1}^{i-1} \mu_0 \cdot \frac{J_{n,k}^{cs}}{\beta_k{}^2} \cdot D3_{n,k} \cdot f3_{n,k}(y) + \mu_0 \cdot \frac{J_{i,k}^{cs}}{\beta_k{}^2} \cdot \begin{bmatrix} C2_{i,k} \cdot f2c_{i,k}(y) \\ \cdots + D2_{i,k} \cdot f2d_{i,k}(y) \\ \cdots + 1 \end{bmatrix} + \sum_{v=i+1}^{Ny} \mu_0 \cdot \frac{J_{v,k}^{cs}}{\beta_k{}^2} \cdot D1_{v,k} \cdot f1_{v,k}(y) \right\} \cdot sin(\beta_k \cdot x) \tag{25}$$

and the component of $\boldsymbol{H_{2_i}}$ (H_{x2_i} and H_{y2_i}) by

$$H_{x2_i} = \sum_k \left\{ \sum_{n=1}^{i-1} \frac{J_{n,k}^{cs}}{\beta_k} \cdot D3_{n,k} \cdot g3_{n,k}(y) + \frac{J_{i,k}^{cs}}{\beta_k} \cdot \begin{bmatrix} C2_{i,k} \cdot g2c_{i,k}(y) \\ \cdots - D2_{i,k} \cdot g2d_{i,k}(y) \end{bmatrix} - \sum_{v=i+1}^{Ny} \frac{J_{v,k}^{cs}}{\beta_k} \cdot D1_{v,k} \cdot g1_{v,k}(y) \right\} \cdot sin(\beta_k \cdot x), \tag{26}$$

$$H_{y2_i} = -\sum_k \left\{ \sum_{n=1}^{i-1} \frac{J_{n,k}^{cs}}{\beta_k} \cdot D3_{n,k} \cdot f3_{n,k}(y) - \frac{J_{i,k}^{cs}}{\beta_k} \cdot \begin{bmatrix} C2_{i,k} \cdot f2c_{i,k}(y) \\ \cdots + D2_{i,k} \cdot f2d_{i,k}(y) \\ \cdots + 1 \end{bmatrix} + \sum_{v=i+1}^{Ny} \frac{J_{v,k}^{cs}}{\beta_k} \cdot D1_{v,k} \cdot f1_{v,k}(y) \right\} \cdot cos(\beta_k \cdot x), \tag{27}$$

where

$$f2c_{i,k}(y) = sh\left[\beta_k \cdot \left(y - y_i^e \right) \right] \Big/ ch(\beta_k \cdot h_{cs}), \tag{28}$$

$$f2d_{i,k}(y) = ch\left[\beta_k \cdot \left(y_i^s - y \right) \right] \Big/ ch(\beta_k \cdot h_{cs}), \tag{29}$$

$$g2c_{i,k}(y) = ch\left[\beta_k \cdot \left(y - y_i^e \right) \right] \Big/ ch(\beta_k \cdot h_{cs}), \tag{30}$$

$$g2d_{i,k}(y) = sh\left[\beta_k \cdot \left(y_i^s - y \right) \right] \Big/ ch(\beta_k \cdot h_{cs}), \tag{31}$$

$$C2_{i,k} = NumC2_{i,k} / Den_{i,k}, \tag{32}$$

$$D2_{i,k} = NumD2_{i,k} / Den_{i,k}, \tag{33}$$

with

$$NumC2_{i,k} = a3_{i,k} \cdot \left(a2_k + a1_k \cdot a4_{i,k} + 1 \right), \tag{34}$$

$$NumD2_{i,k} = \left(a2_k \cdot a3_{i,k} \cdot a4_{i,k} - a1_k \cdot a3_{i,k} + 1 \right), \tag{35}$$

2.4. Correlation FC stack and modeling

The different input data of the model has been listed in Table 1. In could be observed that a conventional PEMFC stack with a constant current I_{fc} of 100 A and an active cell area S_a of 100 cm² is considered.

Table 1. Input parameters of the model adapted to the emulation

Input parameters	Nomenclature	Value in the example [unity]
Fuel cell width	w_{fc}	140 [mm]
Fuel cell height	h_{fc}	140 [mm]
Active surface width	w_{as}	100 [mm]

Active surface height	h_{as}	100 [mm]
Total current	I	100 [A]
Discretization in x-axis	N_x	10 [-]
Discretization in y-axis	N_y	10 [-]
Current density distribution	J_{dis}	N_x by N_y matrix [A/cm^2]

The simplified cross-sectional geometry of the stack is shown in Fig. 4 at the level of one cell. The active part is represented in gray. The current density is considered perpendicular to the cells, keeping a constant value along the stack axis.

The individual segments, of a number of 100, are packaged to simplify the assembly of the device. For convenient operation, the segments are arranged in groups of ten. These parts are named P1 to P10 and located as exposed in Fig. 4. The magnetic field will be recorded using micro-Hall effect sensors. Fig. 4 shows these N_s positions, which could correspond to 60 Hall effect sensors positions (S_0 to S_{Ns}) arranged around the considered FC stack. In order to easily describe the results, the four sides of the FC are numerated.

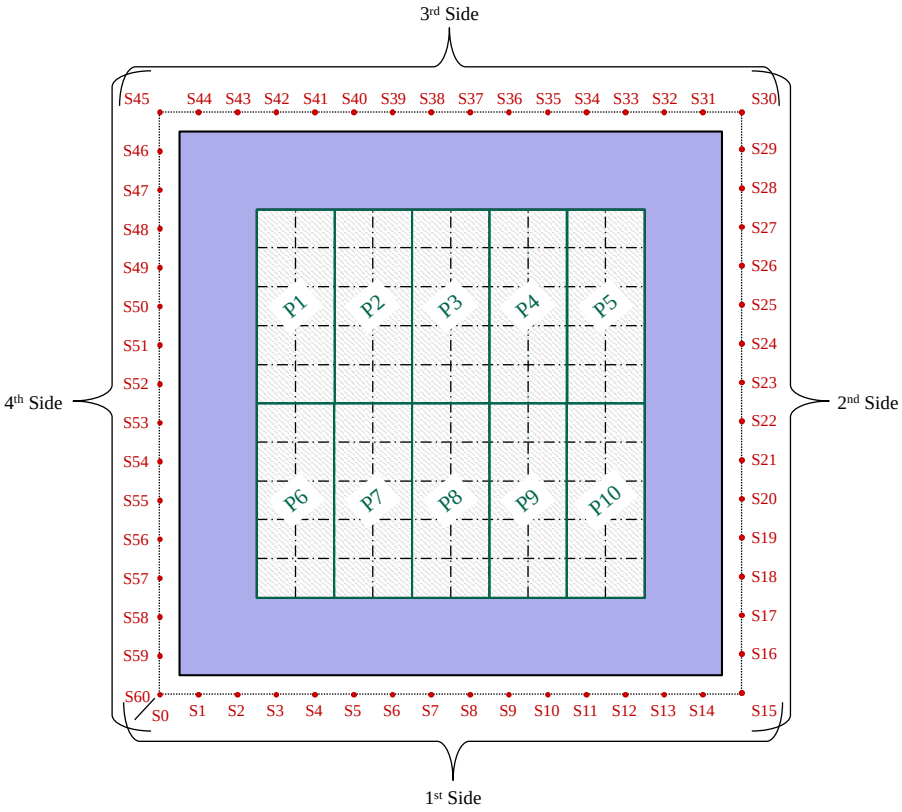

Fig. 4. Global 2-D plan FC discretization with micro-Hall effect sensors.

3. Experimental validation

To evaluate the capacity and efficiency of the 2-D multi-layer model based on the Maxwell-Fourier method, an experimental bench that reproduces the operation of a FC in terms of current density in operating condition is developed [17].

3.1. Material and procedure

In the magnetic context of a fuel cell, the active part is primarily composed of components directly involved in generating the magnetic field associated with the electric current produced by the cell. Key elements typically include the proton exchange membrane (PEM), electrodes (anode and cathode), as well as the bipolar plates.

Emulating the active part with aluminum elements would involve designing an experimental setup capable of replicating the electromagnetic aspects of a fuel cell while utilizing aluminum as the primary material. Injecting current into this setup would allow for simulating various operating conditions, facilitating a thorough analysis of the magnetic behavior.

The considered FC presents an active surface of 10 x 10 = 100 cm². It has been decided to emulate this surface area using square aluminum profiles measuring 1 x 1 = 1 cm², these aluminum segments have a depth of 3 cm. This material has the advantage of being solid, with good electrical conductivity and excellent turning, milling and drilling capabilities. In this way, in preparation for injecting electrical current into the emulated active surface, each segment is pierced and threaded on both sides.

To replicate the electromagnetic functioning of the FC and achieve various current density distributions, it may be necessary to assemble 100 segments arranged to correspond to the shape of the active surface. As a precautionary measure, the segments need to be isolated from each other. For that kapton of 0.02 mm width is used.

The processes with the different steps for the creation of the FC emulator is described using the Fig. 5. The central active part is surrounded by an inactive part with a wide of 20 mm (red frame in Fig. 5). This support is developed using a 3-D printer, in our FCLAB (Fuel Cell LABoratory), as well as the conceptualization and the elaboration of the emulator.

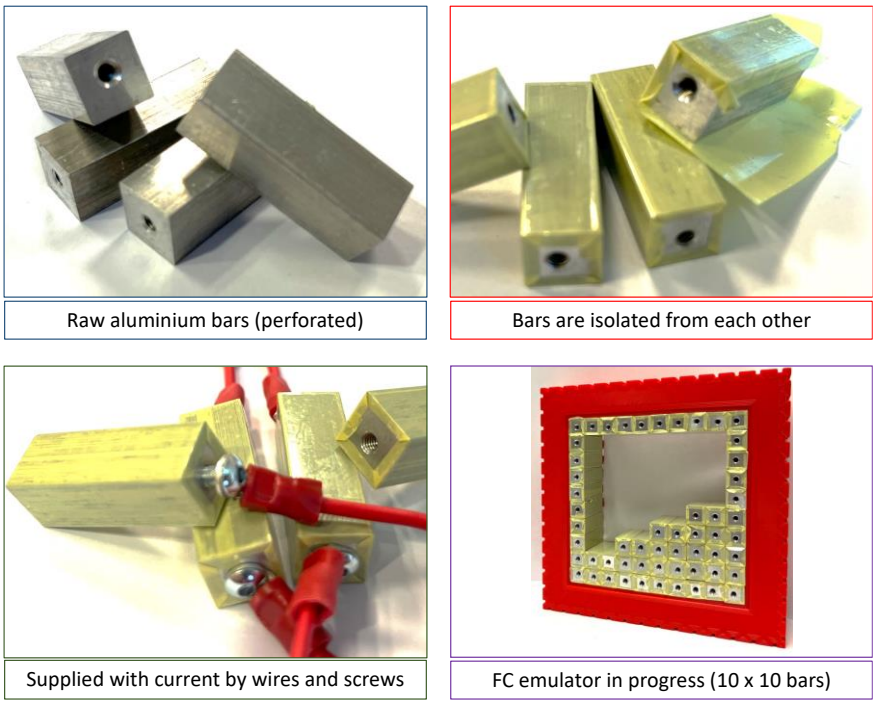

Fig. 5. Processes for FC emulator conception.

3.2. Magnetic field measurement device

One of the first objectives is to measure the magnetic field generated by the FC emulator as a function of the current density distribution. The emulator is surrounded by a non-magnetic

support (3-D printed in white PLA in Fig. 6 and Fig. 7), necessary for the installation of micro-Hall effect sensors. Both components of the magnetic field (viz., normal H_n and tangential H_t) are measured at regular intervals around the FC emulator.

For this purpose, micro-Hall effect sensors HE214T (Asensor Technology AB® [19]) shown in Fig. 6 are used. One of the advantages of this sensor is its thickness, which is only of 0.5 mm. The micro-Hall effect sensor used has 4 pins, 2 to supply the probe with a DC of 1 mA, and 2 to measure the Hall voltage and recover the value of the measured magnetic field. In this way, a circuit board is developed which permits using a basic voltage alimentation (+ 15V, 0V, - 15V), to aliment with a DC current the Hall effect sensor and directly retrieve the Hall voltage.

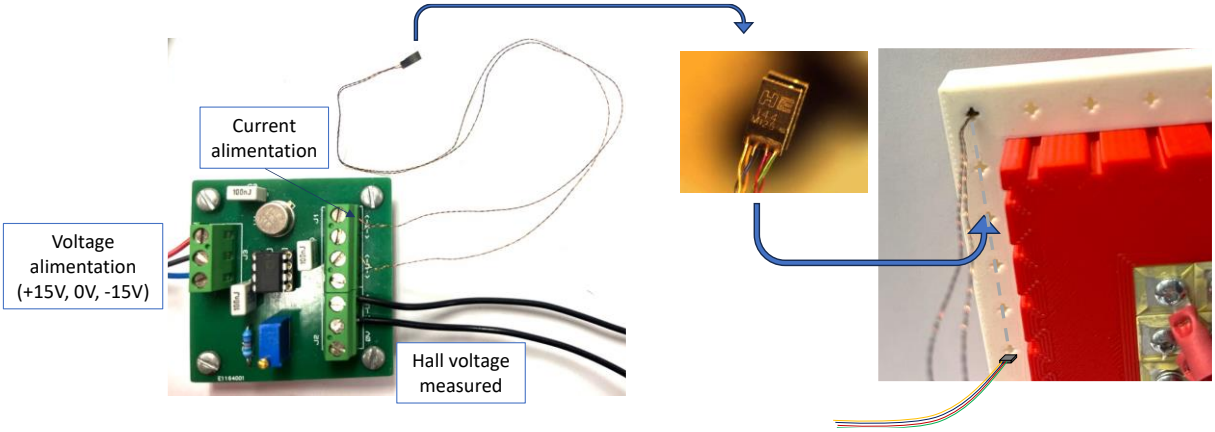

Fig. 6. Micro-Hall effect sensor with his printed board placed in the white which will be displaced around the FC emulator using regular slots (two components).

3.3. Complete emulator and experimental measurements

In order to emulate the current density distribution, the 100 aluminum bars will be supply by DC current, so, the same numbers of wires are connected on each side of each bar which composed the emulator as exposed in Fig. 7. The total electrical current I_{fc} will be maintained to 100 A. Considering a total active surface S_a of 100 cm^2, in nominal conditions, a current I_{cs} of 1 A is distributed in each conductive bar of 1 cm^2.

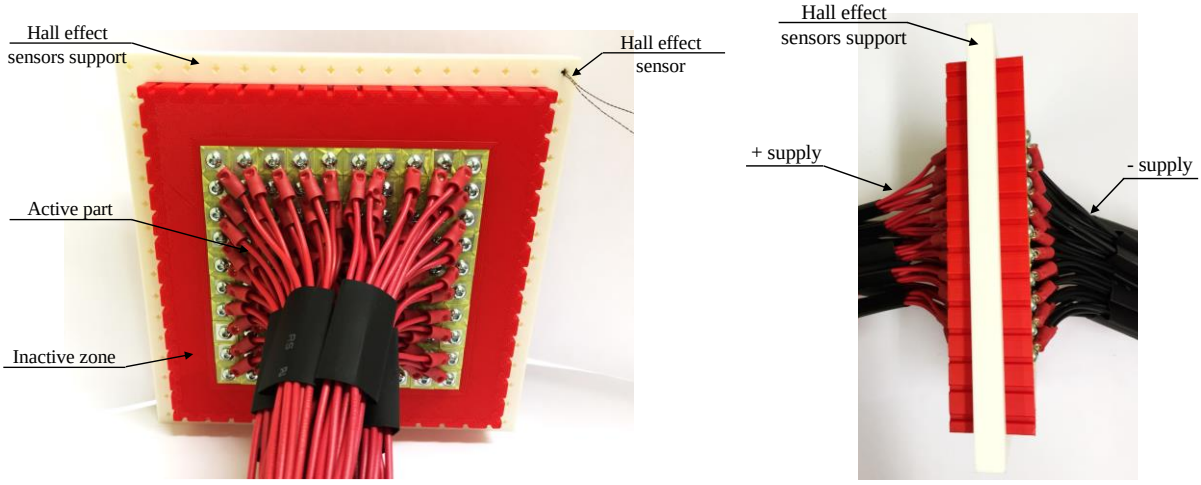

Fig. 7. FC emulator with magnetic measurements device (*x*, *y* view on the left) and (*x*, *z* view on the right).

It is possible to emulate different operating modes, mainly normal and abnormal operation. An abnormal operation as e, consequently, it will result in non-uniform current density

distribution inside the FC emulator. The different parts of the FC emulator, named P1 to P10 in Fig. 4, can be alimented by different value and discretized different. The decrease or increase in current of one or few parts will directly impact the magnetic field distribution around the FC emulator.

4. Results, validation and discussion

4.1. FC current distribution emulation

In this section, the analytical predictions are compared to the experimental measurements. The focus is on the magnetic field waveform around the four sides of the FC. The first comparison is performed for a healthy FC with a homogenous current density J_z of 1 A/cm^2 (as shown in Fig. 8(a)). For an inhomogeneous distribution, different failures are applied with a defective area as presented by current distribution mapping in Fig. 8(b) and (c). In case of a local disparities (Fig. 8(b)), the current density of the damaged part (representing 10 % of the total surface area) is equal to 0.2 A/cm^2 and the rest of the FC is adjusted, keeping a constant total current of 100 A, at 1.09 A/cm^2. For the last current density distribution emulated, a concentration (1.5 A/cm^2) is applied on the left side (representing 20 % of the surface area) and a defective area (0.5 A/cm^2) is considered in the right side (representing also 20 % of the surface area). The rest of the FC emulator surface (60 % of the total surface) keep a current density 1.0 A/cm^2.

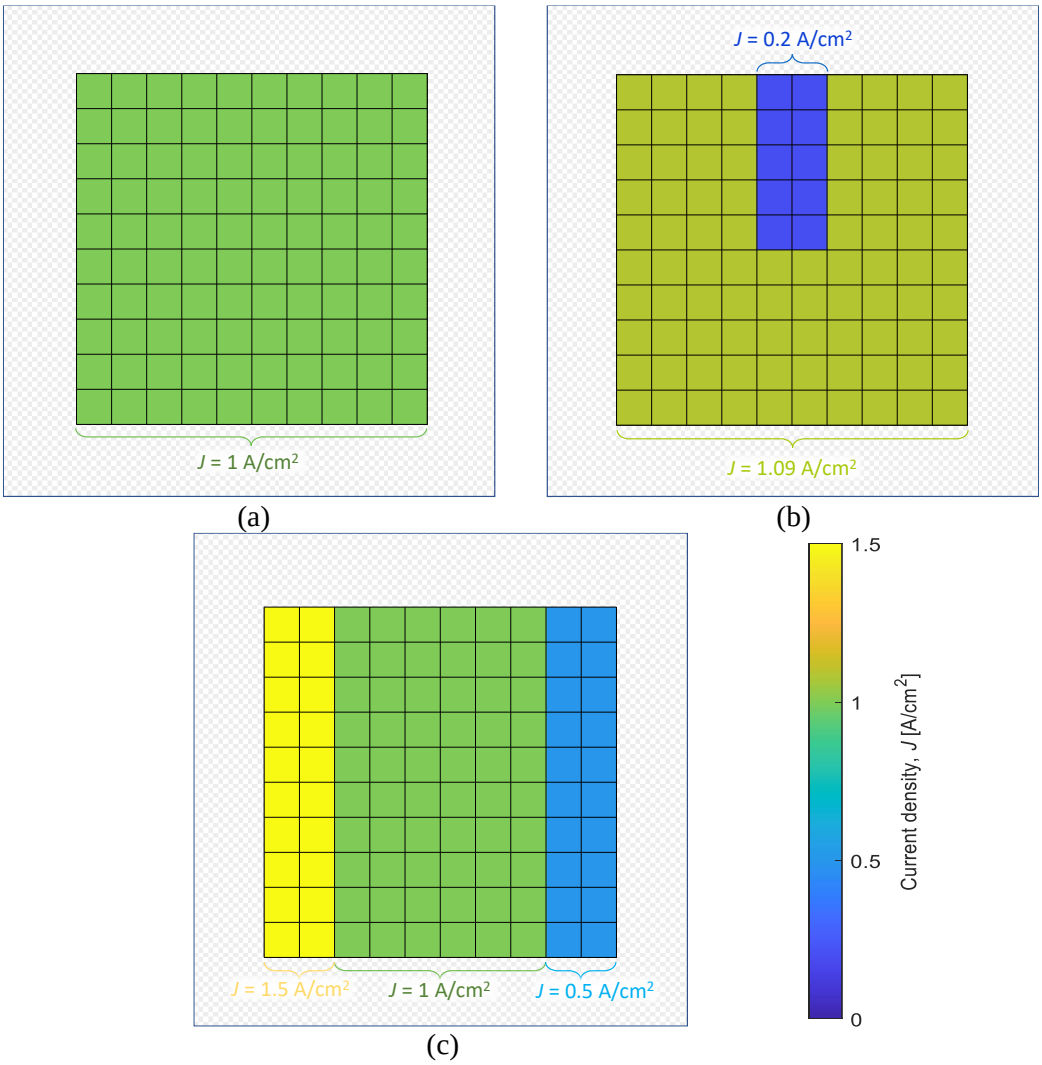

Fig. 8. State of the bipolar plate representation for (a) homogenous current density distribution, (b) local disparity, and (c) distortion on the horizontal side.

The blue areas indicate a reduction in current density, while the yellow areas indicate an increase in current density. The emulation of these changes could be explained by a less active reaction due to insufficient humidity, an uneven gas concentration, a hot spot, etc. In general, a current density defect leads to a reduction in the magnetic field proximate to the impaired zone and an augmentation as one moves away from it. It will be demonstrated in the next section.

4.2. Magnetic field results

In this section, the analytical results are compared to the experimental measurements. The different operating situations (normal case and two abnormal cases) are shown in Fig. 8. Both magnetic field components (i.e., normal H_n and tangential H_t) were measured at regular intervals (every 10 mm). So, this corresponds to 60 experimental measurement points around the FC emulator as exposed in Fig. 4.

The results are compared using Fig. 9. The values of H_n and H_t are plotted for the 60 positions described in Fig. 4. In order to analyze the performance in detail, Fig. 9(a) shows the results of the healthy FC. Fig. 9(b) shows the effects of a 10% defect placed at the top of the FC center (defective P3). Fig. 9(c) shows the results with a concentration in the left (P1 and P6) and a decrease of the current density in the right part of the FC emulator (P5 and P10).

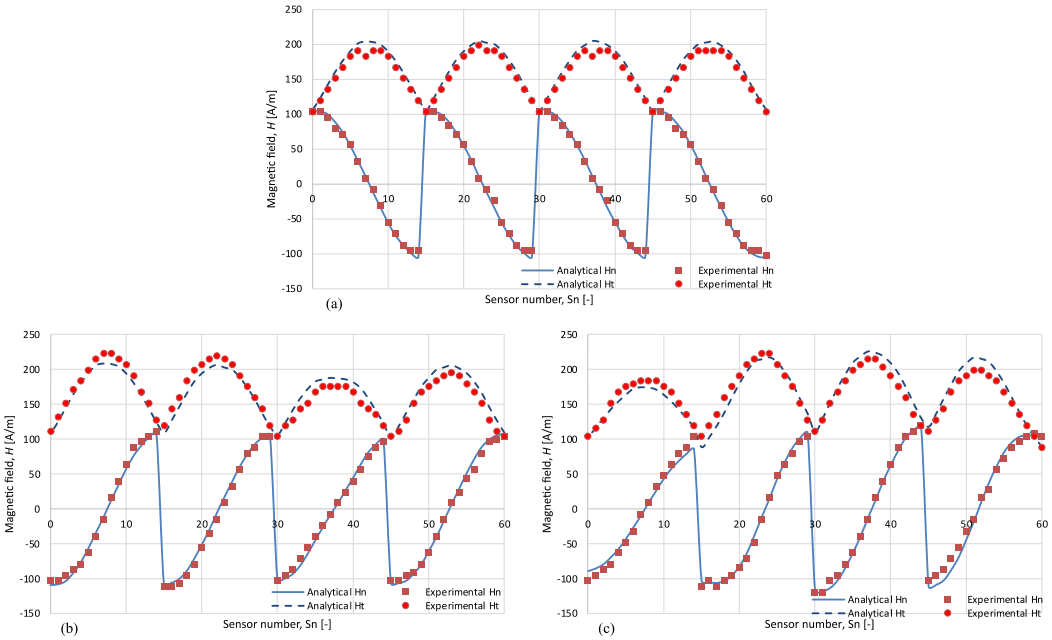

Fig. 9. Magnetic field results comparison for (a) homogenous current density distribution, (b) local disparity, and (c) distortion on the horizontal side.

Overall, the effectiveness of the analytical model is verified since a good accuracy between the experimental measurements and the analytical predictions is undeniable.

For a healthy FC, the magnetic field is the same on the 4 sides of the square formed by the sensors. The two components of the magnetic field of the first sixteen micro-Hall effect sensors (S_0 to S_{15}), corresponding to the 1st side, are similar to the other three sides. In this situation, the experimentally measured magnetic field shows some deviation on the different path (side),

but the trend is respected since the difference does not exceed 10 A/m. The difference could be explained by the uncertainties of the sensor and the measurements devices (Hall effect sensor, amperemeter, voltmeter).

Considering a faulty FC, a magnetic field variation will indicate a fault. In the case of 10 % of the total area of the FC (in Fig. 9(b), the current density of part P3 is maintained to 0.2 A/cm^2), the central sensors of the third path are the most impacted, since these sensors are the closest to the default. Conversely, the more distant sensors exhibit a higher magnetic field than when there is no fault. This is because the total current is maintained at 100 A and the current density of the normal surface is therefore increased (1 A/cm^2 to 1.09 A/cm^2).

Moreover, for the last current density distribution case, the left part has a higher current density (P1 and P6 indicate 1.5 A/cm^2), and in order to compensate for the increase on the left side, a decrease in the current density distribution is emulated on the right side. The current density in the area (P5 and P10) is then 0.5 A/cm^2. Magnetic field distortions mainly affect the closest sensors, namely, path 2 with a decrease and path 4 with an increase. The impact in the magnetic field is more important than the previous case. A correlation can be established between the amount of defective surface and the maximal magnetic field difference.

4.3. Validation analysis

Achieving a high level of accuracy between analytical predictions and experimental measurements will serve to validate the 2-D purely analytical model for both standard and anomalous fuel cell operations.

The provided 5% relative error, when compared to theoretical predictions, is consistently observed. This consistency is largely attributed to inherent uncertainties in the measurement process. It is important to note that measurement data is inherently imprecise, reflecting a fundamental aspect of real experimental measurements.

The experimental measurements were conducted under the assumption that the fuel cell was operating under nominal conditions. However, considering the transient behavior during the operation of a fuel cell is entirely feasible, given that the magnetic field generated by the fuel cell is directly proportional to the current. Quantitatively, there is a higher likelihood of detecting gradual failures at high current levels, as current density disparities are more pronounced under nominal conditions, and this effect is further amplified when the operation is at maximum power. By closely monitoring variations in the magnetic field during these intensive operating conditions, it becomes possible to gain valuable insights into the fuel cell's performance, particularly in identifying early signs of potential failures or malfunctions. This approach allows for a more nuanced assessment of the dynamic behavior of the cell, providing increased opportunities to anticipate and address potential issues under high-load conditions.

To complete about the validation, the different situation representing potentially real case, the possibilities of this model are remarkable and innovative. The authors work on the development of new shape and interesting magnetic field analyzer device adding mu-metal concentrator around the FC. The usual Biot & Savart method, couldn’t be applied with this consideration. Contrary to multi-layer method presented in this paper, which could be easily upgraded into sub-domain method.

The next step is the resolution of the inverse model, this one is under development. The advantage of the multi-layer model is the fast-computing time and a high theoretical precision. Therefore, the use of the inverse model should also lead to obtaining high-quality results while

presenting reduced computation time. In other words, employing this model is expected to achieve high performance while optimizing computational efficiency.

5. Conclusions

In this paper, a new version of an innovative purely analytical model based on the Maxwell-Fourier method is completely described. The experimental setup for the realization of a FC emulator is detailed. Furthermore, the analytical results and the experimental measurements are compared in order to validate the 2-D multi-layer model. The validation is confirmed since the maximal relative error is about 5 %.

The good accuracy exposes the interest of the magneto-tomography for FC diagnosis, and particularly this new purely analytical model. The resolution time corresponds to few seconds, always less than the finite-element analysis. The interest of an analytical model compared to finite-element analysis (except resolution time) is that can be inversed, contrary to numerical methods.

Obviously, the development of a fast and efficient multi-layer model is the first step of the project. An inverse model is under development for the determination of the current density distribution in the FC from the measured magnetic field distribution. Another perspective is to develop a quasi-3-D model to consider the third-dimension influence on the results.

Acknowledgements

This work has been supported by the EIPHI Graduate School (contract ANR-17- EURE-0002) and the Region Bourgogne Franche-Comté.

Références

[1] Gurz M, Baltacioglu E, Hames Y and Kaya K. 2017. The meeting of hydrogen and automotive: a review. Int. J. Hydrogen Energy. 42:23334-23346, doi: 10.1016/j.ijhydene.2017.02.124.

[2] Yue M, Jemei S, Gouriveau R and Zerhouni N. 2019. Review on health-conscious energy management strategies for fuel cell hybrid electric vehicles: degradation models and strategies. Int. J. Hydrogen Energy, 44:6844-6861, doi: 10.1016/j.ijhydene.2019.01.190.

[3] Lorenzo C, Bouquain D, Hibon S and Hissel D. 2021. Synthesis of degradation mechanisms and of their impacts on degradation rates on proton-exchange membrane fuel cells and lithium-ion nickel-manganese-cobalt batteries in hybrid transport applications. Reliab. Eng. Syst. Saf. 212:107369, doi: 10.1016/j.ress.2020.107369.

[4] Rubio MA, Urquia A and Dormido S. 2010. Diagnosis of performance degradation phenomenon in PEM fuel cells. Int. J. Hydrogen Energy. 35:2586-2590, doi: 10.1016/j.ijhydene.2009.03.054.

[5] Chevalier S, Trichet D, Auvity B, Olivier J-C, Josset C and Machmoum M. 2013. Multiphycis DC and AC models of a PEMFC for the detection of degraded cell parameters. Int. J. Hydrogen Energy. 38:11609-11618, doi: 10.1016/j.ijhydene.2013.04.057.

[6] Zheng Z, Petrone R, Péra MC, Hissel D, Becherif M, Pianese C, Steiner N and Sorrentino M. 2013. A review on non-model based diagnosis methodologies for PEM fuel cell stacks and systems. Int. J. Hydrogen Energy. 38:8914-8926, doi: 10.1016/j.ijhydene.2013.04.007.

[7] Geske M, Heuer M, Heideck G, and Styczynski ZA. 2010. Current density distribution mapping in PEM fuel cells as an instrument for operational measurements. Energies. 3:770-783, doi: 10.3390/en3040770.

[8] Hauer KH, Potthast R, Wüster T and Stolten D. 2005. Magneto-tomography-a new method for analysing fuel cell performance and quality. J. Power Source. 143:67-74, doi: 10.1016/j.jpowsour.2004.11.054.

[9] Lustfeld H, Reißel M, Schmidt U and Steffen B. 2009. Reconstruction of electric currents in a fuel cell by magnetic field measurements. J. Fuel Cells Sci. Technol. 6:Art. ID 021012, doi: 10.1115/1.2972171.

[10] Nasu T, Matsushita Y, Okano J and Okajima K. 2012. Study of current distribution in PEMFC stack using magnetic sensor probe. Journal of International Council on Electrical Engineering. 2:391-396, doi: 10.5370/JICEE.2012.2.4.391.

[11] Le Ny M, Chadebec O, Cauffet G, Dedulle JM, Bultel Y, Rosini S, Fourneron Y and Kuo-Peng P. 2013. Current distribution identification in fuel cell stacks from external magnetic field measurements. IEEE Trans. Magn. 49:1925-1928, doi: 10.1109/TMAG.2013.2239967.

[12] Ifrek L, Chadebec O, Rosini S, Cauffet G, Bultel Y and Bannwarth B. 2019. Fault identification on a fuel cell by 3-D current density reconstruction from external magnetic field measurements. IEEE Trans. Magn. 55:Art. ID 6200705, doi: 10.1109/TMAG.2019.2895755.

[13] Katou T, Gotoh Y, Takahashi N and Izumi M. 2012. Measurement technique of distribution of power generation current using static magnetic field around polymer electrolyte fuel cell by 3D inverse problem FEM. Materials Transactions. 53:279-284, doi: 10.2320/matertrans.I-M2011842.

[14] Yamanashi R, Gotoh Y, Izumi M and Nara T. 2015. Evaluation of generation current inside membrane electrode assembly in polymer electrolyte fuel cell using static magnetic field around fuel cell. ECS Trans. 65:219-226, doi: 10.1149/06501.0219ecst.

[15] Plait A, Giurgea S, Hissel D and Espanet C. 2020. New magnetic field analyzer device dedicated for polymer electrolyte fuel cells noninvasive diagnostic. Int. J. Hydrogen Energy. 45:14071-14082, doi: 10.1016/j.ijhydene.2020.03.082.

[16] Plait A and Dubas F. 2022. A 2D Multi-Layer Model to Study the External Magnetic Field Generated by a Polymer Exchange Membrane Fuel Cell. Mathematics. 10:3883, doi: 10.3390/math10203883

[17] Plait A and Dubas F, 2022. Experimental validation of a 2-D multi-layer model for fuel cell diagnosis using magneto-tomography. In Proceeding 23rd World Hydrogen Energy Conference (WHEC), Istanbul, Turkey, June 26-30.

[18] Dubas F and Boughrara K. 2017. New scientific contribution on the 2-D subdomain technique in Cartesian coordinates: Taking into account of iron parts. Math. Comput. Appl. 22:p17, doi: 10.3390/mca22010017.

[19] Asensor Technology AB, Linear High Precision Analog Hall Sensors. https://www.asensor.eu.